
Learning Continuous Rotation Canonicalization with Radial Beam Sampling

Johann Schmidt and Sebastian Stober
Artificial Intelligence Lab, Faculty of Computer-Science
Otto-von-Guericke University
Universitätsplatz 2, 39106 Magdeburg, Germany
{johann.schmidt, stober}@ovgu.de

Abstract

Nearly all state of the art vision models are sensitive to image rotations. Existing methods often compensate for missing inductive biases by using augmented training data to learn pseudo-invariances. Alongside the resource demanding data inflation process, predictions often poorly generalize. The inductive biases inherent to convolutional neural networks allow for translation equivariance through kernels acting parallelly to the horizontal and vertical axes of the pixel grid. This inductive bias, however, does not allow for rotation equivariance. We propose a radial beam sampling strategy along with radial kernels operating on these beams to inherently incorporate center-rotation covariance. Together with an angle distance loss, we present a radial beam-based image canonicalization model, short BIC. Our model allows for maximal continuous angle regression and canonicalizes arbitrary center-rotated input images. As a pre-processing model, this enables rotation-invariant vision pipelines with model-agnostic rotation-sensitive downstream predictions. We show that our end-to-end trained angle regressor is able to predict continuous rotation angles on several vision datasets, *i.e.* *FashionMNIST*, *CIFAR10*, *COIL100*, and *LFW*. Our code is publicly available at github.com/johSchm/RadialBeams.

1 Introduction

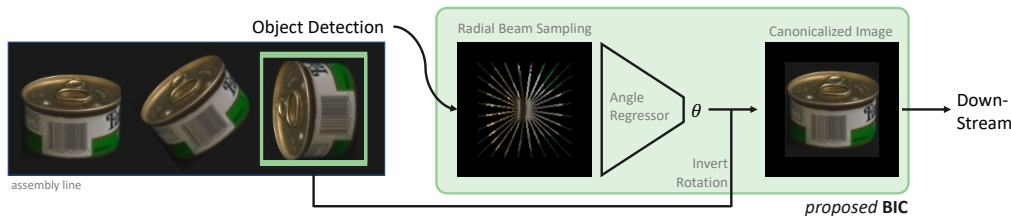


Figure 1: Industrial Radial Beam-based Image Canonicalization (BIC) application setting.

Computers often struggle to detect the high-level semantic similarity between center-rotated objects, a task trivial to humans. During the rotation transformation the structure (semantic similarity) of the object is preserved. We say the center-rotation is a symmetry of that object. Ignoring these symmetries, which are embedded in our world would confront us with tons of semantically redundant information. The human brain learns to discard these symmetry transformations [20] to free its immanent representations from these redundancies. From an Information Theoretical point of view, avoiding redundancies allows for a more efficient usage of computing capacities. With this at hand, we can argue from an human cognition and mathematical perspective for an increased leverage of symmetries in novel deep learning architectures. A logical first step involves integrating *a priori* known symmetries in our artificial systems.

In this work, we narrow down the scope to the image processing pipeline. CNNs (Convolutional Neural Networks) revolutionized the computer vision field and now they are indispensable in modern deep learning [1]. This is grounded on the reduced parameter footprint through shared filter parameters and spatially-independent feature detection, which introduced translation equivariance to CNNs (proof provided by Cohen and Welling [5]). Although, translation equivariant architectures are a major step towards efficient vision models many known visual symmetries are disregarded. In this work, we aim to extend the symmetry scope of vision pipelines by rotation invariance. Generally, three options exist of how to integrate invariances/equivariances in deep learning models:

(i) Integrate an inductive bias, which renders the architecture inherently invariant/equivariant to the target symmetry. Equivariance limits the function space to valid models under the rules of natural image formation [29], which supports learning and generalization. For instance, most attempts to integrate rotation equivariance in CNNs [5, 33, 7] are non-trivial, come with decisive constraints in the filter space, and are limited to discrete rotation groups.

(ii) Augment the training set by sampling from the symmetry orbits (see Sec. 2) and hence inflate the dataset by *e.g.* rotated versions of the vanilla image [4]. During training, the network learns to approximate these orbits on the latent manifold (pseudo-equivariance) or collapse them (pseudo-invariance). While being straightforward, this poses a massive increase on the required sample complexity to cover the symmetry space sufficiently. In Sec. 3 we pursue a more profound investigation in the related work.

(iii) Alternatively, a surjective projection during pre-processing can be used to collapse the orbit of an image to its canonical form. The *terminus technicus* for this technique is canonicalization, which we investigate in this work. Specifically, we design a continuous angle regressor able to estimate the rotation angle of input images. This should answer the question: *Given an arbitrary center-rotated image, what is its canonicalized orientation?* The model learns image canonicalization and hence maps all possible rotations of an image, *i.e.*, the image orbit, to a single orientation. In practise, our model is placed between an object detector and a rotation sensitive downstream model, as illustrated in Fig. 1. The object detection acts as an additional symmetry reducer by pruning all but the relevant pixel information. Our model does not pose any restriction in terms of the downstream task or model used. All this is based on our core idea of radial beam sampling, where we sample beams of pixels originating from the center of the image to its edge region. This introduces a covariance between center-rotations of the underlying image and circular shifts of the sampled beams. We propose an inductive bias, which embeds this covariance into the encoder of our proposed BIC model. Compared to the work of Keller and Welling [15], this covariance does not need to be learned. Our model approximates the full rotational Lie group, rather than limited discrete rotation subgroups as of prior works [7, 26]. Compared to rotation-equivariant inductive biases [9], our approach does not bound the hypothesis class and simultaneously lowers the sample complexity of the downstream model. We provide more methodological details in Sec. 4, which we thoroughly evaluate in Sec. 5.

2 Symmetries and Group Theory

A symmetry of an object is a transformation that preserves the structure of the object, like the 120° rotation of an equilateral triangle. Mathematically, symmetries of an object are comprised in a group, *i.e.*, a set with an operation. Therefore, the rotations keep the structure of the triangle form a discrete group containing $0^\circ, 120^\circ$ and 240° . Besides discrete symmetry groups, Lie groups are continuous symmetry groups whose elements form a smooth differentiable manifold, like the rotation group of a circle. Of uttermost interest of this paper are real two-dimensional rotations described by the Special Orthogonal Group $SO(2)$. This group comprises distance-preserving transformations of the Euclidean space, which is an essential property for image rotations. Formally, the group is defined by

$$SO(2) = \left\{ \mathfrak{g} : \rho(\mathfrak{g}) = R_\theta \equiv \begin{bmatrix} \cos(\theta) & -\sin(\theta) \\ \sin(\theta) & \cos(\theta) \end{bmatrix} \Big|_{+360^\circ} \right\}, \quad (1)$$

where the rotation angle $\theta \in [0^\circ, 360^\circ)$ is expressed by the group algebra \mathfrak{g} . $\rho(\mathfrak{g})$ is called the representation of \mathfrak{g} , *i.e.*, the rotation matrix. The group operation $+_{360^\circ}$ indicates $\text{mod}(360^\circ)$, such that, for instance, $220^\circ +_{360^\circ} 150^\circ = 10^\circ$. Acting with each group element on an object forms a set of outputs, which is called the orbit of this object. For an arbitrary group \mathfrak{G} we have, $\text{orb}(x, \mathfrak{G}) = \{\rho(\mathfrak{g})x \mid \mathfrak{g} \in \mathfrak{G}\}$, where x denotes the query object. A function f (*e.g.*, modelled by a neural network), which follows the symmetry group \mathfrak{G} , is either equivariant, invariant, or covariant [22]. Out of these three categories, covariance is the most general one, where $f(\rho(\mathfrak{g})x) = \rho'(\mathfrak{g})f(x), \forall \mathfrak{g} \in \mathfrak{G}$. Both transformations might be potentially different on their domain and co-domain, respectively. From this definition, we can derive

the following two special cases: If the output stays unaltered after transforming the input, $f(\rho(\mathbf{g})x) = f(x), \forall \mathbf{g} \in \mathfrak{G}$, we call f invariant. If the output is transformed equally, $f(\rho(\mathbf{g})x) = \rho(\mathbf{g})f(x), \forall \mathbf{g} \in \mathfrak{G}$, we call f equivariant. For more details please refer to Bronstein *et al.* [3]. In this work we strive after continuous rotation invariances following the full Lie group $SO(2)$. As shown in the related work, however, most rotation symmetric vision networks respect only narrow subgroups of $SO(2)$.

3 Related Work

Through its simplicity, the process of augmenting training data is a prevalent strategy to learn more robust models. For that, the dataset is augmented with samples from the loss-preserving symmetry orbit of a datapoint, like rotations of a base image. During training pseudo-invariances are supposed to be embedded into the latent manifold by learning proximity regions of pseudo-invariant data points in the latent space. Goodfellow *et al.* [10] show that the quality of pseudo-invariance in the learned representation increases with the depth of the network. Minor deformations and transformations, like shifts and rotations, are attenuated by lower layers, while invariances are progressively formed by higher layers. As shown by Shuxiao Chen *et al.* [4] and Dao *et al.* [6] augmentation acts as a regularizer penalizing model complexity by learning to minimize the average over loss signals under the group actions. Despite these benefits, modern networks already depend on massive training datasets full of semantic redundancies, whose sample complexity is even enlarged by additional augmentation processes. Alternatively to the hard-won pseudo-invariances, inductive biases open the gates for true invariances [23]. Gens and Domingos [9] leverage the aforementioned proximity regions of invariant datapoints by enforcing layers to deliberately model the symmetry space of inputs. Hence, points propagated through the network can be pooled with their closest neighbors (*i.e.*, their symmetry transformed replicates) and mapped to the same output label. Max Jaderberg *et al.* [14] ingrain jointly learned transformations to CNNs, which project inputs to their canonical representations. This, however, is limited to small perturbations of inputs. Hu *et al.* [12] constrain filters to symmetric weight matrices, *i.e.*, isotropic filters. This also reduces the memory footprint since only a sub-matrix needs to be stored. Cohen and Welling [5] expand the symmetry range of CNNs to reflections and integer multiples of 90° rotations around the center. Zhou *et al.* [33] decompose weight matrices into learnable weight vectors and meta-learned (binary) symmetry matrices. Ecker *et al.* [7] represent kernels in a steerable basis modelled by 2D Hermite polynomials to allow for weight sharing across kernel orientations. Build upon these results, Ustyuzhaninov *et al.* [26] canonicalize the kernel weights for different orientations. The majority of proposed methods drastically constrain the filter space, which renders arbitrary visual feature learning impossible. Furthermore, due to the finite number of kernel matrices and rotational artifacts, only a limited number of discrete rotations is supported. Both drawbacks are eliminated with our proposed method.

4 Methodology

We present an orientation canonicalizer for image data. At its heart our model uses radial beams sampled from the input image as illustrated in Fig. 2. This is followed by an angle regressor as shown in Fig. 3. The predicted angle is used to canonicalize the input image using back-rotation. Let $X \in \mathcal{X}(\Omega)$ be an image on the pixel grid domain Ω sampled from the dataset \mathcal{X} . Particularly, we have an image tensor $X \in \mathbb{R}^{W \times H \times C}$ with width W , height H , and color channels C . In practice, we use batched data but for brevity, we drop the batch dimension in this article.

Radial Beam Sampling Conventional convolution on image data uses horizontally and vertically aligned rectangular kernels *w.r.t.* Ω . This allows for translation equivariance when shifting the object along either of these axes. In this work, we are interested in center-rotations of images rather than translations. We argue that one way to enable rotation equivariance is to alter the alignment of kernels. To this end, we utilize kernels operating along beams radiating from the center to the edges of the image. Formally, a beam b is a fixed vector radiating from $[\lfloor \frac{W}{2} \rfloor, \lfloor \frac{H}{2} \rfloor]$ with length D and a certain direction.

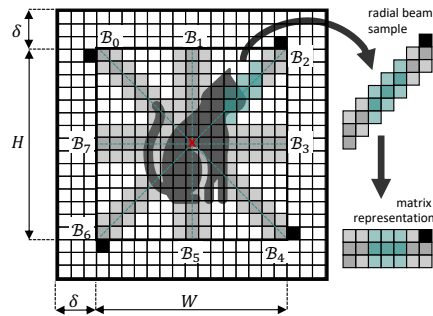


Figure 2: Exemplary beam set \mathcal{B} on the padded image X . Beams are highlighted in grey, where a lighter color indicates the thickness ϵ and black the padded pixels. The radial convolutional kernel iterating over a beam is highlighted in cyan.

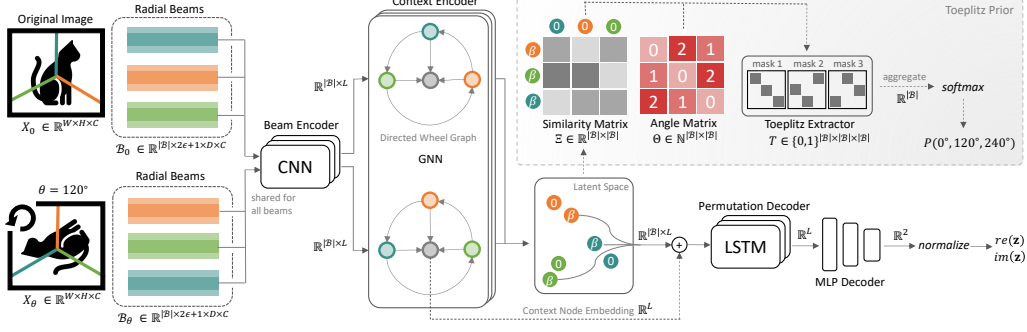


Figure 3: Schematic illustration of our BIC angle regressor. The proposed Toeplitz prior for training utilizes a contrastive setting of X_0 and the θ -rotated X_θ . First, radial beams \mathcal{B}_0 and \mathcal{B}_θ are sampled with proximity, which are embedded by a shared CNN encoder. To encode neighborhood information of adjacent beams, a Graph Neural Network (GNN) is utilized. During training time, a prior on the resulting latent manifold can be imposed. To that end, a pairwise similarity matrix Ξ over embeddings of \mathcal{B}_0 and \mathcal{B}_θ is computed. We show that θ is mapped to diagonals in Ξ . Leveraging this insight, we can extract the probability over discrete rotations from this matrix by using a Toeplitz extractor T conditioned on the angle matrix Θ . During inference, however, we are limited to a single input image X_θ . To find the rotation angle of that image, we leverage the permutation of beam embeddings, which are decoded by a Long Short Term Memory (LSTM) followed by a Multi-Layer Perceptron (MLP). We use a complex unit vector regression by jointly predicting the real and imaginary parts.

We use a deterministic sampling strategy to obtain a radial beam set \mathcal{B} , as illustrated in Fig. 2. Since this is a rigid overlay mask on top of Ω , beam positions are agnostic to any image X . This allows us to check for intersections of $\mathbf{b} \in \mathcal{B}$ with the pixel grid Ω once. Afterwards, we only need to extract the color information of image X at these positions to evaluate the beams. In practice, this can be implemented via the Bresenham Algorithm [2]. The cardinality $|\mathcal{B}|$ is a hyper-parameter, which is upper-bounded by $|\mathcal{B}_{max}|$, which is defined in the Lemma below. Beams are spaced equally from another to obtain a near uniform receptive field and reduce bias in the sampling. Note that beams occupy a certain spatial region. We control the thickness of beams by $\epsilon \in \mathbb{N}$. To this end, we modify the classical Bresenham Algorithm and add additional neighborhood pixels, such that with $\epsilon = 1$ the sampled line is enlarged by a border of one pixel to both sides, increasing the width to $2\epsilon + 1$. For more details, please refer to App. C or our source code. To further understand the information density extracted from X by \mathcal{B} , we propose an approximation of the beam coverage and the resulting overlaps *w.r.t.* $|\mathcal{B}|$ and length D .

Lemma 1. *The pixel coverage Γ_{cover} of radial beams sampled from image X is given by*

$$\Gamma_{cover}(|\mathcal{B}|, D) \approx |\mathcal{B}| \left[\frac{4D^2}{|\mathcal{B}|} - \frac{\left(\frac{8D}{|\mathcal{B}|} - (2\epsilon + 1)\right)^2}{2 \tan\left(\frac{360^\circ}{|\mathcal{B}|}\right)} \right]. \quad (2)$$

Then, the pixel overlap Γ_{over} can be estimated by

$$\Gamma_{over}(|\mathcal{B}|, D) \approx |\mathcal{B}| \left[(2\epsilon + 1)D + \frac{\left(\frac{8D}{|\mathcal{B}|} - (2\epsilon + 1)\right)^2}{2 \tan\left(\frac{360^\circ}{|\mathcal{B}|}\right)} - \frac{4D^2}{|\mathcal{B}|} \right]. \quad (3)$$

Lemma 2. *The maximum number of beams is*

$$|\mathcal{B}_{max}| \approx \sqrt{\frac{64D^2}{(2\epsilon + 1)^2}}, \quad (4)$$

which is an exact maximum for $\epsilon = 0$ and an approximation otherwise.

The proofs are stated in App. D.1 and App. D.2, respectively.

Shared Beam Encoder We embed the sampled beams using a shared beam encoder, which we also use to mitigate coarsening issues, as we will describe in the following. Through the trigonometrical

functions \sin and \cos in Eq. (1), the rotation matrix R can take real values even for integer angles. Mapping the rotated pixel positions back to the coarse pixel grid introduces two problems: (i) Pixels might end up outside the pixel grid, where specifically the corners of images are at risk. This can be circumvented by isotropic zero-padding and thus increasing the image size to $W + 2\delta$ and $H + 2\delta$.

Lemma 3. *The optimal padding δ for any squared image X , which obviates any information loss when rotating X under group transforms in $SO(2)$, is given by*

$$\delta = \max\left(0, \left\lceil \frac{1}{2}W(\sqrt{2}-1) \right\rceil\right). \quad (5)$$

The proof is stated in App. D.3. Note that the padding has no effect on the prediction and is only used to prevent information loss during group transformations. (ii) Rotations also introduce rounding errors on Ω . Due to the real matrix R and the discrete pixel grid, an integer constraint must be enforced after rotation. Thus, destination locations of pixels might be allocated multiple times where others are missed completely. To mitigate these artifacts, we smoothen the rotation by bilinear interpolation between pixels. For further mitigation, we leverage the proximity around each pixel. The beam encoder embeds the proximity-aided beam evaluations in a latent representation, *i.e.*, $\mathbf{b} \in \mathbb{R}^{2\epsilon+1 \times D} \rightarrow \mathbb{R}^L$, where L is the latent space dimensionality.

Context Encoder The representation emerging from the beam encoder ties spatial information together with color values. Since this is done individually for each beam, we mitigate greedy decisions by incorporating the spatial context through a GNN. See App. B for more details on GNNs. The context encoder is modelled by a directed wheel graph with $|\mathcal{B}| + 1$ nodes. The graph topology chosen encodes two important properties to the information exchange during representation learning. First, we leverage direct links to the center node of the wheel graph to aggregate messages from all beam nodes. Therefore, the center node representation will hold the full global context. Secondly, we use undirected links emerging in the directed circle of beam nodes. We deliberately chose undirected over bidirected links to bypass graph isomorphisms. Particularly, the spatial information of whether an adjacent node is above or below is crucial to quantify rotations. This also allows us to mitigate over-smoothing [21] by holding back the global context and adding it after the GNN. In App. F.2 we give more technical details, for instance, regarding the message passing strategy.

Toeplitz Prior We aim to predict the rotation angle given the beam representations obtained after both encoding steps. We achieve this by utilizing contrastive input tuples (X_0, X_θ) and learn clusters of similar beam embeddings, where $X_\theta = R_\theta X_0$ with $R_\theta \in \mathcal{C}_{|\mathcal{B}|}$. $\mathcal{C}_{|\mathcal{B}|}$ is a subgroup of $SO(2)$, such that

$$\mathcal{C}_{|\mathcal{B}|} = \left\{ R_\theta : \theta = \frac{k}{|\mathcal{B}|} 360^\circ \mid k \in \{0, 1, \dots, |\mathcal{B}| - 1\} \right\}. \quad (6)$$

In other words, we rotate images during training only by angles between two beams (not necessarily adjacent ones). Since beams are represented by a tensor \mathcal{B} , each beam $\mathbf{b} \in \mathcal{B}$ has a certain position in \mathcal{B} . Without loss of generality, we set the first beam as the upper left one. In this light, rotating by $R_\theta \in \mathcal{C}_{|\mathcal{B}|}$ will shift/roll the positions of beams in \mathcal{B} (see Fig. 3). This introduces a bijection between k and θ , such that rotations in the ambient space are mapped to circular shifted beam embeddings. Hence, we need to quantify by how many positions the beams are shifted to infer the image rotation. For that, we compute a similarity matrix Ξ using all pairwise beam combinations. We measure the similarities between beam embeddings by $1/(1 + \|\cdot\|_2)$. Diagonals in Ξ are coherent to circular shifts of beams in \mathcal{B} . We assign to each element in Ξ the respective circular shift value (k in Eq. (6)). This gives the angle matrix Θ as illustrated in Fig. 3. Θ is a Toeplitz matrix, where elements on each diagonal are set to their respective k . We can extract diagonals by a Toeplitz extraction tensor T or short Toeplitz extractor. Intuitively, this is a collection of $|\mathcal{B}|$ binary matrices masking the diagonals of Ξ . This allows us to filter out the similarity scores for each possible discrete rotation in $\mathcal{C}_{|\mathcal{B}|}$. Now, all scores per rotation can be summed up and we can compute the probability for each rotation

$$u_k = \mathbf{1}^\top (\Xi \odot T_k) \mathbf{1} \quad \text{and} \quad p(k) = \frac{e^{u_k}}{\sum_{j=0}^{|\mathcal{B}|-1} e^{u_j}}, \quad (7)$$

where u_k is the logit score of k , $p(k)$ its probability, $\mathbf{1}$ is a one-vector of length $|\mathcal{B}|$ and \odot denotes the Hadamard product. Due to the *a priori* defined T this prior is fully differentiable.

Decoding The Toeplitz prior enforces a deliberate structure on the latent manifold (sketched in Figure Fig. 3). During inference, this structure needs to be leveraged to determine rotation angles of single input images X_θ without the constrastive X_0 . Since the set of beams is represented as a tensor, an order is enforced. We build upon the assumption that during training a structured latent manifold is learned on which the order of context-aware beams infer rotation information. During inference, we utilize this permutation of X_θ and decode the sequence of beams using a LSTM. This is followed by linear transformations, such that the decoder maps $\mathbb{R}^{|\mathcal{B}|\times L} \rightarrow \mathbb{R}^L \rightarrow \mathbb{R}^2$.

Unit Circle Loss Instead of predicting a real number indicating θ , we leverage the specific structure of angle data, which has its origin on the complex plane. Let \mathbf{z} be a complex vector on the unit circle. As stated in complex analysis, the angle between the positive real axis and \mathbf{z} is $\arg \mathbf{z} = \theta$, such that each \mathbf{z} maps to a θ . The argument of \mathbf{z} can be computed as $\arg(\mathbf{z}) = \text{atan2}(\text{im}(\mathbf{z}), \text{re}(\mathbf{z}))$, where $\text{im}(\mathbf{z})$ and $\text{re}(\mathbf{z})$ are the imaginary and real part of \mathbf{z} , respectively. Predicting \mathbf{z} will bound the predicted angle to $[0^\circ, 360^\circ)$ and introduce smooth transitions from 359° to 0° . In practice, we normalize the output of the final linear layers to the unit length $\mathbf{z}/\|\mathbf{z}\|_2$. Eventually, a loss is required which penalizes the predicted unit vector \mathbf{z} *w.r.t.* its ground truth angle θ on the unit circle. We use the squared error between the real and imaginary parts such that

$$\mathcal{L}_{circle}(\theta, \mathbf{z}) = (\sin(\theta) - \text{im}(\mathbf{z}))^2 + (\cos(\theta) - \text{re}(\mathbf{z}))^2. \quad (8)$$

The unit circle loss is a highly expressive loss function, since it preserves angle distances as we show in App. E.1. We prove bounds in App. E.2 and show that this is Lipschitz smooth in App. E.3. The Toeplitz prior acts via a supplementary loss term, such that

$$\mathcal{L}(\theta, \mathbf{z}, P) = \mathcal{L}_{circle}(\theta, \mathbf{z}) + \mathcal{L}_{prior}(\theta, P) \quad \text{with} \quad \mathcal{L}_{prior}(\theta, P) = \sum_{i=0}^{|\mathcal{B}|-1} P_\theta^{(i)} \log P^{(i)}, \quad (9)$$

where P_θ is a one-hot vector of length $|\mathcal{B}|$ that indicates the true rotation angle θ . P is the predicted distribution using the Toeplitz prior pipeline (see Eq. (7)).

5 Experiments

Unless stated explicitly, we use the following setup for all experiments: The beam encoder is partitioned into a proximity encoder and a spatial encoder. The proximity encoder uses 2D convolutional kernels shifting over each beam and compresses the signal down to a latent subspace $\mathbb{R}^{|\mathcal{B}|\times 2\epsilon+1\times D\times C} \rightarrow \mathbb{R}^{|\mathcal{B}|\times D-8\times L/8}$. We use valid padding for all convolutions to reduce the dimensionality. The subsequent beam encoder processes the embedding with 1D spatial convolution $\mathbb{R}^{|\mathcal{B}|\times D-8\times L/8} \rightarrow \mathbb{R}^{|\mathcal{B}|\times L}$. We use a 128-dimensional latent space (*i.e.*, $L = 128$). The context and neighborhood information among beams is encoded using a three-layer GNN. The obtained embeddings and their ordering are decoded in a three-layer LSTM, representing the permutation decoder $\mathbb{R}^{|\mathcal{B}|\times L} \rightarrow \mathbb{R}^L$. We utilize *LeakyReLU* activations as piece-wise non-linearities, *i.e.*, $\max(0.3x, x)$, which empirically found to be more performant than *ReLU*s. Weight initialization according to He *et al.* [11] is used with a bias initialization close to 0 to accompany the rectified network well. Eventually, three linear layers and a subsequent normalization transform the final latent state of the permutation decoder to a complex vector $\mathbb{R}^L \rightarrow [-1, 1]^2$. Find more details in App. F or in our source code.

We use mini-batches of 128 elements for training with $|\mathcal{B}| = 32$ beams per image and a thickness of $\epsilon = 1$. We use a split of 80% training, 10% validation, and 10% test data. Each dataset is augmented by randomly center-rotated replicas of the original data points. To this end, we sample $\theta \sim \mathcal{U}(\{360^\circ |\mathcal{B}|^{-1} k : k \in \{0, 1, \dots, |\mathcal{B}| - 1\}\})$. As we will show in the following, our model is able to generalize well to the test data. Therefore, *no* explicit regularization is utilized, like dropout or specific loss terms. We use the popular Adam optimizer [16] with a static learning rate of 0.0001, momentum terms $\beta_1 = 0.9$ and $\beta_2 = 0.999$ to update the model parameters. We perform several experiments on four vision datasets, *i.e.* *FashionMNIST* [30], *CIFAR10* [19], *COIL100* [24], and *LFW* [13]. Our experiments are structured as follows: In Sec. 5.1 we analyse the latent structure imposed by the prior. We vary the receptive field of the model and test out-of-distribution (OOD) predictions in Sec. 5.2. In Sec. 5.3 we vary the pixel space dimensions and analyse the performance of our model. We investigate the translation robustness of BIC in Sec. 5.4. Finally, we analyse downstream predictions in Sec. 5.5 to support our initial motivation given in Sec. 1.

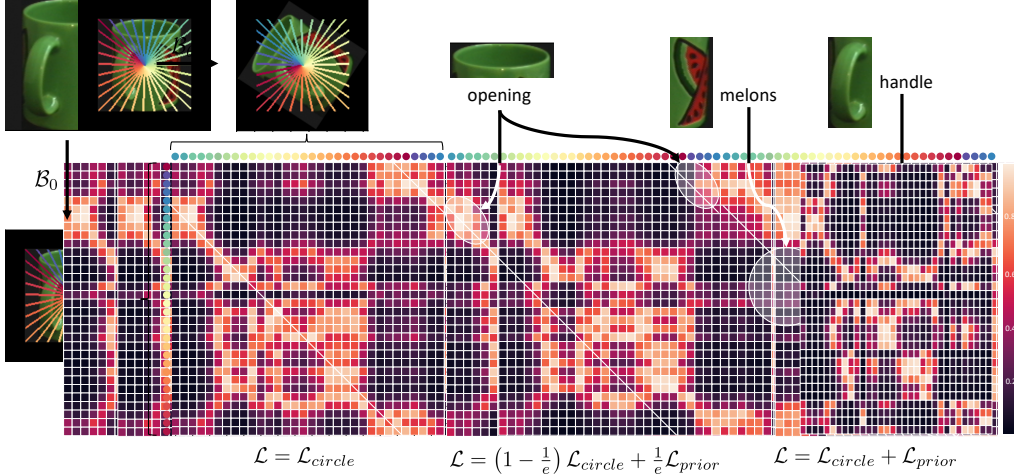


Figure 4: Similarity matrix Ξ of an image sample obtained from the *COIL100* dataset using different training losses. Core feature patches are highlighted along with the ground truth diagonals.

5.1 Imposed Latent Structure

The core purpose of the Toeplitz prior is to explicitly impose structure in the latent space and hence ease learning. Specifically, the optimization objective aims to form a target pattern in the similarity matrix Ξ as aforementioned. Surprisingly, we found during our experiments that such a prior is not required and the intended geometric structure is learned by the circle loss alone. We trained our model using the complete loss definition in Eq. (9), a linear combination of both loss terms *w.r.t.* the epoch e , and no Toeplitz prior at all. In Fig. 4, we depict the similarity matrices for all three objectives, where analog geometric structures emerge independent of the Toeplitz prior. The latent structure should also accompany our hypothesis that image rotations cohere with circular shifts of beam embeddings. We test this by computing the beam embeddings of the entire group orbit of $\mathcal{C}_{|\mathcal{B}|}$. The beam embeddings should form a surface topologically equivalent to a circle. Fig. 5 shows the 2D *t-SNE* [27] projection (see App. G.1 for more details about the setup). The representation resembles of a Möbius strip indicating exactly the looked after continuity. With these empirical findings, we claim that a training without \mathcal{L}_{prior} suffices. Due to the scale sensitivity of the prior, we are now more independent on the target group \mathcal{C} , which we will exploit in following experiments.

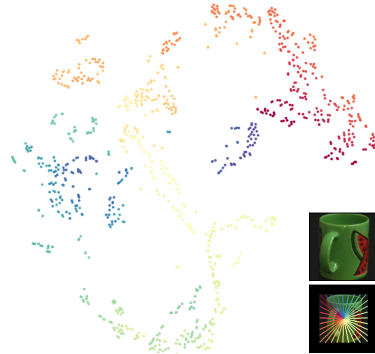


Figure 5: 2D non-linear projection of beam embeddings using *t-SNE* comprising all beams of the sample image's $\mathcal{C}_{|\mathcal{B}|}$ orbit.

5.2 Receptive Field and OOD Predictions

How many beams \mathcal{B} are required for sufficiently low prediction errors? We hypothesize that the smaller the receptive field the lower the prediction performance. Conceptually, the thickness ϵ scales the local receptive field, whereas $|\mathcal{B}|$ is the parameter to tune for global perception. In our experiments, we concentrate on $|\mathcal{B}|$ and keep $\epsilon = 1$. We test our hypothesis on the *COIL100* dataset, which eliminates the abuse of background noise. Further, due to its relatively large pixel grid we have more options in $|\mathcal{B}|$. We test on the finite group $\mathcal{C}_{|\mathcal{B}|}$, which scales with $|\mathcal{B}|$ (see Eq. (6)). Fig. 6A shows the test performance of our BIC both trained and tested on $\mathcal{C}_{|\mathcal{B}|}$ using different number of beams. As the results indicate, the test circle loss converges faster to a smaller local minimum with larger $|\mathcal{B}|$. The more beams we use to sample the image, the higher the input information density and therefore, the more fine-grained decisions about the exact rotation angle can be made. Inputs outside the finite training group $\mathcal{C}_{|\mathcal{B}|}$ are referred to as OOD. Without the bijection between beams and discrete rotations, the model has to interpolate between angles. The smaller $|\mathcal{B}|$, the wider is the interpolation distance. The violin plot in Fig. 6B represents the test performance on $\mathcal{C}_{|\mathcal{B}_{max}|}$ using a model trained on $\mathcal{C}_{|\mathcal{B}|}$. As

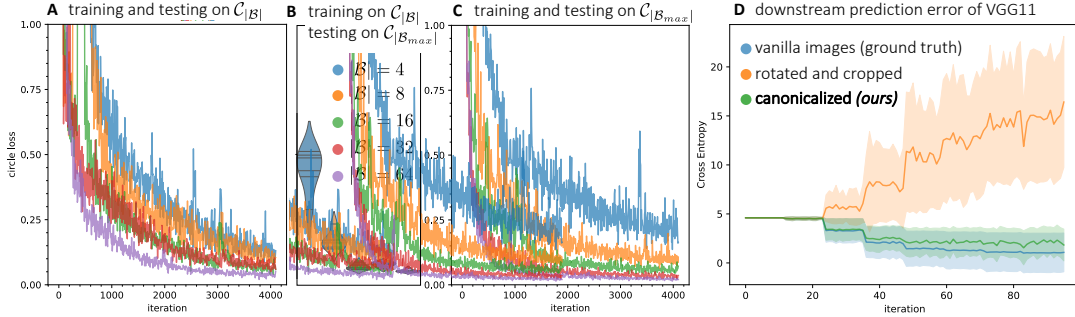


Figure 6: Performance results on *COIL100*. **A** Test performance with the same rotation group $\mathcal{C}_{|\mathcal{B}|}$ used for training and testing. **B** Test performance when trained on $\mathcal{C}_{|\mathcal{B}|}$ and tested on $\mathcal{C}_{|\mathcal{B}_{max}|}$. **C** Test performance with the same rotation group $\mathcal{C}_{|\mathcal{B}_{max}|}$ used for training and testing. **D** Shows the class-accumulated and batch-averaged cross entropy on the test set using a *VGG11* over five runs.

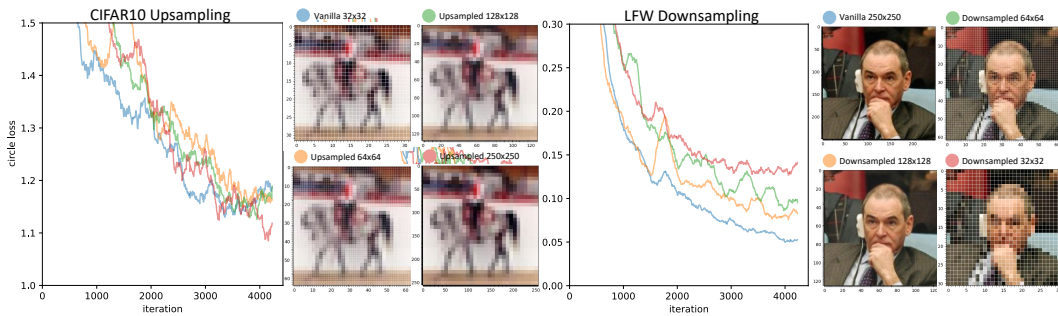


Figure 7: Test performance using upsampled *CIFAR10* images and downsampled *LFW* images.

Table 1: Test performance after 4096 training batches using the base setup and five runs per dataset.

Dataset	Cardinality	BIC Memory	Image Shape	D	\mathcal{L}_{circle}
FashionMNIST [30]	60,000	2.02 MB	$28 \times 28 \times 1$	14	0.2605 ± 0.0011
CIFAR10 [19]	60,000	2.19 MB	$32 \times 32 \times 3$	16	0.6372 ± 0.0097
COIL100 [24]	7,200	2.24 MB	$128 \times 128 \times 3$	64	0.0601 ± 0.0001
LFW [13]	13,000	2.25 MB	$250 \times 250 \times 3$	125	0.0592 ± 0.0001

expected, the model performs significantly better on the test set using larger $|\mathcal{B}|$ since less interpolation is needed. The same holds when analysing the test performance when trained and tested on $\mathcal{C}_{|\mathcal{B}_{max}|}$, as depicted in Fig. 6C. Since our beam encoder embeds each beam in a latent representation, all subsequent components are invariant to beam length D . This manifests in the slight memory increase in Table 1. Still, all model variations have only around 0.025% of the memory footprint of common vision models, like the *VGG16* [25].

5.3 Scalability to varying pixel spaces

As illustrated in Table 1, our BIC model particularly struggles with lower-resolution datasets, like *FashionMNIST* or *CIFAR10*. We hypothesize that this originates from the *de facto* denser sampled input space (due to the higher cardinality along with the smaller pixel grid). Since samples are closer in the input space, individual canonical orientations are harder to distinguish. We eliminated the impact of the encoder on the prediction difference by downsampling images in *LFW* and upsampled images in *CIFAR10* with nearest neighbor resampling. In this way, information is unaltered during upsampling but a more powerful encoder is utilized to cope with the increased pixel grid. Fig. 7 (left) shows no significant performance change. Hence, the reason for the overall low performance on *CIFAR10* is not due to the encoder. In the light of this hypothesis, downsampling images in *LFW* up to the grid size of *CIFAR10* should come with a performance drop. This is in fact shown in Fig. 7 (right), where lowering the number of pixels, *i.e.*, information, reduces the performance. But still, BIC performs better on the

32×32 downsampled *LFW* than on 32×32 vanilla *CIFAR10*. Hence, the above reasoning holds and we can argue that this is indeed due to sample complexity. To this end, we would need more training epochs and larger parameter spaces considering the standard sample complexity lower bound. Thus, we conclude that sampling beams with small D renders exact angle regression difficult.

5.4 Geometric Stability to Translations

In a real world setting, input images might be perturbed by small translations. BIC is not translation equivariant due to the radial sampling radiating from the center. We view BIC as a part of a larger machine vision pipeline, where this drawback might be compensated by other components. However, for a robust machine vision pipeline, our model has to fend off these small perturbations, since exact upstream invariances are unlikely in real world settings. In theory, geometric stability to signal deformations is measured by a continuous complexity measure [3]. In this analysis, we use a subgroup of the translation group $T(2)$, which contains transformations respecting the discrete pixel grid, *i.e.*, $T(2, \Omega) \subset T(2)$. The violin plot in Fig. 8 shows the test performance decrease when translating the query images horizontally and vertically. Angle predictions below the 5° stability boundary are maximally 5° off from the unperturbed predictions. Considering the mean of the predictions, we conclude that our BIC model is geometrically stable up to ± 3 pixels. This can be improved by an increased thickness ϵ , which we have set to 1 for our experiments.

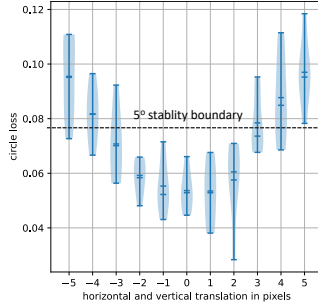


Figure 8: Translation robustness on the test set of *COIL100*.

5.5 Downstream Evaluation

Since BIC is thought as a pre-processing model, we test its impact on a downstream image classifier. As the downstream model will be fed by the canonicalized images (through back-rotation) we smoothen the rotation by bilinear interpolation between pixels. We choose *VGG11* [25] as a classical image classifier to act as the downstream model. We infer from Fig. 6D that *VGG11* trained on *COIL100* is able to fit the vanilla test set (*blue*). However, it is incapable of properly classifying rotated replicates of the test set (*orange*). These are cropped to fit Ω , which does not cause any information loss (due to the padding). Inverting the rotation by our proposed BIC model, on the other hand, enables near optimal test predictions (*green*).

6 Conclusion

We presented an angle regressor for image data based on radial beams sampled from the input image. Our proposed pre-processing model Radial Beam-based Image Canonicalization (BIC) maps arbitrary center-rotated images to their canonicalized orientations. This allows for model-agnostic rotation-sensitive downstream prediction networks. Through the deliberate integration of inductive biases, we achieved a comparatively modest memory footprint with roughly 0.025% of common vision models, like *VGG16*. During our investigations, we found that our circle symmetry-preserving loss already learns a meaningful structured latent space and therefore does not require explicit priors like the presented Toeplitz prior. We provided evidence that the required group orbits emerge in the latent space. Besides empirical findings, we present mathematical proofs for the proposed radial beam sampling procedure. Building upon these findings, potential future work might investigate the information decrease along a beam towards the center, *i.e.*, pixels further from the center are more effected by rotations than pixels closer to the center. This, however, is not encoded when using weight-sharing radial kernels as used in our work. Furthermore, handling redundancies emerging from beam overlaps might open space for future works.

Acknowledgments

The authors acknowledge the financial support by the Federal Ministry of Education and Research of Germany (BMBF) within the framework for the funding for the project SENECA.

References

- [1] Simone Bexten, Johann Schmidt, Christoph Walter, and Norbert Elkmann. Human action recognition as part of a natural machine operation framework. In *2021 26th IEEE International Conference on Emerging Technologies and Factory Automation (ETFA)*, pages 1–8, 2021. doi: 10.1109/ETFA45728.2021.9613331.
- [2] Jack Bresenham. Algorithm for computer control of a digital plotter. *IBM Syst. J.*, 4:25–30, 1965.
- [3] Michael M. Bronstein, Joan Bruna, Taco Cohen, and Petar Veličković. Geometric deep learning: Grids, groups, graphs, geodesics, and gauges, 2021.
- [4] Shuxiao Chen, E. Dobriban, and Jane Lee. Invariance reduces variance: Understanding data augmentation in deep learning and beyond. *ArXiv*, abs/1907.10905, 2019.
- [5] Taco S. Cohen and Max Welling. Group equivariant convolutional networks, 2016.
- [6] Tri Dao, Albert Gu, Alexander Ratner, Virginia Smith, Chris De Sa, and Christopher Re. A kernel theory of modern data augmentation. In Kamalika Chaudhuri and Ruslan Salakhutdinov, editors, *Proceedings of the 36th International Conference on Machine Learning*, volume 97 of *Proceedings of Machine Learning Research*, pages 1528–1537. PMLR, 09–15 Jun 2019. URL <https://proceedings.mlr.press/v97/dao19b.html>.
- [7] Alexander S. Ecker, Fabian H. Sinz, Emmanouil Froudarakis, Paul G. Fahey, Santiago A. Cadena, Edgar Y. Walker, Erick Cobos, Jacob Reimer, Andreas S. Tolias, and Matthias Bethge. A rotation-equivariant convolutional neural network model of primary visual cortex, 2018.
- [8] Francesco Farina and Emma Slade. Symmetry-driven graph neural networks, 2021.
- [9] Robert Gens and Pedro Domingos. Deep symmetry networks. In *Proceedings of the 27th International Conference on Neural Information Processing Systems - Volume 2*, NIPS’14, page 2537–2545, Cambridge, MA, USA, 2014. MIT Press.
- [10] Ian J. Goodfellow, Quoc V. Le, Andrew M. Saxe, Honglak Lee, and Andrew Y. Ng. Measuring invariances in deep networks. In *Proceedings of the 22nd International Conference on Neural Information Processing Systems*, NIPS’09, page 646–654, Red Hook, NY, USA, 2009. Curran Associates Inc. ISBN 9781615679119.
- [11] Kaiming He, Xiangyu Zhang, Shaoqing Ren, and Jian Sun. Delving deep into rectifiers: Surpassing human-level performance on imagenet classification, 2015. URL <https://arxiv.org/abs/1502.01852>.
- [12] Xu Shell Hu, Sergey Zagoruyko, and Nikos Komodakis. Exploring weight symmetry in deep neural networks, 2019.
- [13] Gary B. Huang, Manu Ramesh, Tamara Berg, and Erik Learned-Miller. Labeled faces in the wild: A database for studying face recognition in unconstrained environments. Technical Report 07-49, University of Massachusetts, Amherst, October 2007.
- [14] Max Jaderberg, Karen Simonyan, Andrew Zisserman, and Koray Kavukcuoglu. Spatial transformer networks, 2016.
- [15] T. Anderson Keller and Max Welling. Topographic vaes learn equivariant capsules. *ArXiv*, abs/2109.01394, 2021.
- [16] Diederik P. Kingma and Jimmy Ba. Adam: A method for stochastic optimization. *CoRR*, abs/1412.6980, 2015.
- [17] Thomas N. Kipf and Max Welling. Semi-supervised classification with graph convolutional networks, 2017.
- [18] Risi Kondor, Hy Truong Son, Horace Pan, Brandon Anderson, and Shubhendu Trivedi. Covariant compositional networks for learning graphs, 2018.
- [19] Alex Krizhevsky. Learning multiple layers of features from tiny images. 2009.

- [20] Joel Z Leibo, Jim Mutch, and Tomaso Poggio. Learning to discount transformations as the computational goal of visual cortex. 2011. doi: <https://doi.org/10.1038/npre.2011.6078.1>.
- [21] Qimai Li, Zhichao Han, and Xiao-Ming Wu. Deeper insights into graph convolutional networks for semi-supervised learning, 2018. URL <https://arxiv.org/abs/1801.07606>.
- [22] Diego Marcos, Michele Volpi, Nikos Komodakis, and Devis Tuia. Rotation equivariant vector field networks. In *2017 IEEE International Conference on Computer Vision (ICCV)*. IEEE, oct 2017. doi: 10.1109/iccv.2017.540. URL <https://doi.org/10.1109/iccv.2017.540>.
- [23] Seth Nabarro, Stoil Ganev, Adria Garriga-Alonso, Vincent Fortuin, Mark van der Wilk, and Laurence Aitchison. Data augmentation in bayesian neural networks and the cold posterior effect. *ArXiv*, abs/2106.05586, 2021.
- [24] Sheila J. Nayar. Columbia object image library (coil100). 1996.
- [25] Karen Simonyan and Andrew Zisserman. Very deep convolutional networks for large-scale image recognition, 2014. URL <https://arxiv.org/abs/1409.1556>.
- [26] Ivan Ustyuzhaninov, Santiago A. Cadena, Emmanouil Froudarakis, Paul G. Fahey, Edgar Y. Walker, Erick Cobos, Jacob Reimer, Fabian H. Sinz, Andreas S. Tolias, Matthias Bethge, and Alexander S. Ecker. Rotation-invariant clustering of neuronal responses in primary visual cortex. In *International Conference on Learning Representations*, 2020. URL <https://openreview.net/forum?id=rklr9kHFDB>.
- [27] Laurens van der Maaten and Geoffrey E. Hinton. Visualizing data using t-sne. *Journal of Machine Learning Research*, 9:2579–2605, 2008.
- [28] Boris Weisfeiler and A. A. Lehman. A Reduction of a Graph to a Canonical Form and an Algebra Arising During This Reduction. *Nauchno-Tekhnicheskaya Informatsia*, Ser. 2(N9):12–16, 1968.
- [29] Daniel E. Worrall, Stephan J. Garbin, Daniyar Turmukhambetov, and Gabriel J. Brostow. Harmonic networks: Deep translation and rotation equivariance. In *2017 IEEE Conference on Computer Vision and Pattern Recognition (CVPR)*, pages 7168–7177, 2017. doi: 10.1109/CVPR.2017.758.
- [30] Han Xiao, Kashif Rasul, and Roland Vollgraf. Fashion-mnist: a novel image dataset for benchmarking machine learning algorithms, 2017. URL <https://arxiv.org/abs/1708.07747>.
- [31] Keyulu Xu, Weihua Hu, Jure Leskovec, and Stefanie Jegelka. How powerful are graph neural networks?, 2019.
- [32] Manzil Zaheer, Satwik Kottur, Siamak Ravanbakhsh, Barnabas Poczos, Russ R Salakhutdinov, and Alexander J Smola. Deep sets. In I. Guyon, U. V. Luxburg, S. Bengio, H. Wallach, R. Fergus, S. Vishwanathan, and R. Garnett, editors, *Advances in Neural Information Processing Systems*, volume 30. Curran Associates, Inc., 2017. URL <https://proceedings.neurips.cc/paper/2017/file/f22e4747da1aa27e363d86d40ff442fe-Paper.pdf>.
- [33] Allan Zhou, Tom Knowles, and Chelsea Finn. Meta-learning symmetries by reparameterization, 2021.

A Nomenclature

A.1 Acronyms

BIC	Radial Beam-based Image Canonicalization
CNN	Convolutional Neural Network
GNN	Graph Neural Network
LSTM	Long Short Term Memory
MLP	Multi-Layer Perceptron
OOD	out-of-distribution

A.2 Symbols

Symbol	Description
X	Image
\mathcal{X}	Image dataset
Ω	Pixel grid domain
W	Width of an image
H	Height of an image
C	Color channels of an image
\mathcal{B}	Beam set
\mathcal{B}_{max}	The maximal beam set
$ \mathcal{B} $	Beam set cardinality
$b \in \mathcal{B}$	A single beam
D	Beam length
θ	Rotation angle
Θ	Angle matrix (see Fig. 3 for a visual illustration)
R_θ	Rotation matrix with angle θ
\mathfrak{S}	Some symmetry group
$SO(2)$	Special Orthogonal Group
$\mathcal{C}_{ \mathcal{B} }$	Discrete rotation group with $ \mathcal{B} $ elements
\mathfrak{g}	Group element
ρ	Group representation
T	Toeplitz extractor (see Fig. 3 for a visual illustration)
Ξ	Similarity matrix (see Fig. 3 for a visual illustration)
ϵ	Thickness of beams
δ	Image padding size
L	Latent dimension

B Graph Neural Networks

GNNs (Graph Neural Networks) enable learning on graphs and thus directly leverage the underlying data structure as an inductive bias. The basis for this is a learnable inference method, *i.e.* the iterative parameterized message passing procedure. By virtue of simplicity, we consider only graph convolutional neural networks [17], which we will use interchangeably with GNNs in this work. Furthermore, we use node and vertex as synonyms, as well as edge and link to denote connections. At each layer l the node features of each node are updated by the GNN propagation rule

$$\mathbf{h}_v^{l+1} \leftarrow f_{node} \left(\bigcirc_{u \in \mathcal{N}(v)} f_{link}(\mathbf{h}_v^l, \mathbf{h}_u^l), \mathbf{h}_v^l \right), \quad (10)$$

where \mathbf{h}_v^{l+1} is the updated node embedding (output of layer l). \bigcirc denotes a permutation invariant operation, like summation, maximization, minimization, or averaging [32]. This is the reason for GNN being permutation invariant *w.r.t.* their local node set. Therefore, graphs convey the underlying topology not the geometry, *i.e.* distances and angles between nodes. With this we encode the symmetry of graphs, such that the fact that nodes are connected is crucial not the spatial positions of nodes. This however, is not always beneficial since its worsening the representational power and causes steerability downsides for some use cases [18]. Although, mean and max-pooling aggregators are well-defined multiset functions, they are not injective [31]. For multiset injective aggregators, this learning procedure closely resembles the well-known Weisfeiler-Lehman Graph Isomorphism Test [28]. This test provides an answer to the questions to whether or not two graphs are topologically equivalent. Note, however, that the outcome of this test provides a necessary but insufficient condition for graph isomorphisms. As shown in [31], especially the sum operator holds the highest expressiveness among permutation invariant aggregator choices.

Farina and Slade [8] proposed an angle preserving graph network, which encodes the direction of the neighbor nodes. For $l=0$ we initialize \mathbf{h}_v^l by the node features \mathbf{x}_v . This update mechanism is a composition of a node embedding function f_{node} and a link embedding function f_{link} , where both are modelled by neural networks rendering the procedure learnable. f_{link} models the message passing procedure, where the query node embedding \mathbf{h}_v^l and its neighbor node embedding \mathbf{h}_u^l are combined in a non-linear fashion. This allows for an information flow from the neighbor nodes $\mathcal{N}(v)$ of query node v to itself. In Eq. (10) we used the sum operator as the aggregator of all messages. The result is passed into the node embedding function f_{node} also modelled by a neural network, which encodes the aggregated information and the current query node embedding. Node states are propagated until a equilibrium is obtained. This iterative convolutional process allows for a treatment of irregular data.

C Bresenham's Line Algorithm for Radial Beam Sampling

Algorithm 1 Bresenham's Line Algorithm for line thickness $\epsilon = 1$ and arbitrary angles. The thickness is represented by two additional lines (one left and one right border line).

Require: strictly positive pixel space spanned by horizontal axis h and vertical axis v
Require: start point $x \in \mathbb{N}^2$
Require: end point $y \in \mathbb{N}^2$
Require: swapped = *false*
Require: line = $[[[], [], []]]$ ▷ arrays for left border, main line, right border

- 1: $dh = y_0 - x_0$ ▷ difference first coordinate
- 2: $dv = y_1 - x_1$ ▷ difference second coordinate
- 3: $m = |dv| > |dh|$ ▷ store original slope
- 4: **if** m **then** ▷ reflection along $v = h$ if it is too steep, which will reduce the slope *w.r.t.* h
- 5: $(x_0, x_1) \leftarrow (x_1, x_0)$
- 6: $(y_0, y_1) \leftarrow (y_1, y_0)$
- 7: **end if**
- 8: **if** $x_0 > x_1$ **then** ▷ swap start and end point to achieve right directed lines
- 9: $(x_0, y_0) \leftarrow (y_0, x_0)$
- 10: $(x_1, y_1) \leftarrow (y_1, x_1)$
- 11: swapped = *true*
- 12: **end if** ▷ we have $\angle(\overline{xy}, h) \in [-45^\circ, 45^\circ]$ and the line points away from the origin
- 13: $dh \leftarrow y_0 - x_0$ ▷ re-calculate difference first coordinate
- 14: $dv \leftarrow y_1 - x_1$ ▷ re-calculate difference second coordinate
- 15: $e = \text{int}(dx/2)$ ▷ used to determine when a vertical step is needed
- 16: **if** $y_0 < y_1$ **then** ▷ determine steps along v
- 17: $ds = 1$ ▷ $\angle(\overline{xy}, h) \in [-45^\circ, 0^\circ]$
- 18: **else**
- 19: $ds = -1$ ▷ $\angle(\overline{xy}, h) \in [0^\circ, 45^\circ]$
- 20: **end if**
- 21: **for** $i \in [x_0, y_0]$ **do** ▷ step along the horizontal dimension of the line
- 22: **if** m **then** ▷ switch according to original line
- 23: line[1][i] = (y, x) ▷ add point to main line
- 24: $a = (y - 1, x)$ ▷ first border point
- 25: $b = (y + 1, x)$ ▷ second border point
- 26: **else**
- 27: line[1][i] = (x, y) ▷ add point to main line
- 28: $a = (x, y - 1)$ ▷ first border point
- 29: $b = (x, y + 1)$ ▷ second border point
- 30: **end if**
- 31: **if** swapped or m **then**
- 32: line[0][i] = b ▷ add left border point
- 33: line[2][i] = a ▷ add right border point
- 34: **else**
- 35: line[0][i] = a ▷ add left border point
- 36: line[2][i] = b ▷ add right border point
- 37: **end if**
- 38: $e \leftarrow e - |dv|$
- 39: **if** $e < 0$ **then** ▷ step in on the vertical axis
- 40: $y \leftarrow y + s$
- 41: $e \leftarrow e + dh$
- 42: **end if**
- 43: **end for**
- 44: **return** line

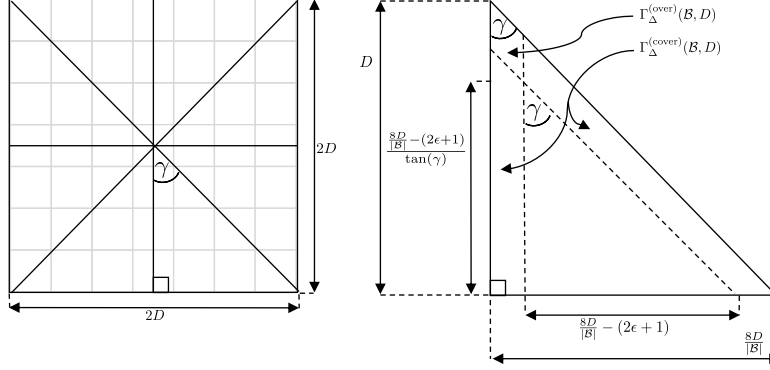


Figure 9: (left) Exemplary beam sketch with $|\mathcal{B}|=8$ on the pixel grid Ω . Each beam has a fixed length of D , thus a two-dimensional hull of length and height $2D$ results. (right) One example triangle with base length and height annotated with the deduced formulas, as well as the coverage $\Gamma_{\Delta}^{(\text{cover})}(|\mathcal{B}|, D)$ and overlap $\Gamma_{\Delta}^{(\text{over})}(|\mathcal{B}|, D)$. Within the triangle, beam widths are depicted by dashed lines.

D Proofs

D.1 Beam Overlaps and Coverage Approximation

Proof. We use a linear relaxation of the discrete pixel grid to quantify the coverage and overlap. Under the assumption of reflection symmetric beams, where we can position the symmetry axis at every beam and opposite beam pair (see Fig. 9). Therefore, the space is chopped into equally sized triangles. It is sufficient to estimate quantities for one triangle and extrapolate to the full scope. Let $\gamma = 360^\circ / |\mathcal{B}|$ be the angle of each triangle at the center of the image. We can leverage the spatial bound of any new beams, which is hemmed in by its adjacent neighbors. We say that a pixel of a beam either overlaps another beam's pixel or not. As aforementioned all beam lengths are limited to D pixels. Let $\Gamma_{\Delta}^{(\text{cover})}, \Gamma_{\Delta}^{(\text{over})} \in \mathbb{R}_+$ be the coverage and overlap of triangle Δ , respectively. The coverage is a strict upper bound for the overlap $\Gamma_{\Delta}^{(\text{cover})} > \Gamma_{\Delta}^{(\text{over})}$ since the last pixel of any beam needs to be unique otherwise the beam already exists in \mathcal{B} . Intuitively, the narrower the neighbors, the tighter the spatial bound, the higher the overlap. The base length of each triangle can be computed by

$$\frac{2D}{\frac{1}{4}|\mathcal{B}|} = \frac{8D}{|\mathcal{B}|}. \quad (11)$$

Part of the approximation is the assumption that all are orthogonal triangles. Under the linear relaxation we can compute the surface area of an triangle by

$$\Delta(\mathcal{B}, D) = \frac{1}{2} \frac{8D}{|\mathcal{B}|} D = \frac{4D^2}{|\mathcal{B}|}. \quad (12)$$

The surface area of the inner embedded triangle, *i.e.*, the uncovered area, can be computed using different trigonometric ratios. Here, we leverage the fact that γ appears also as the top angle of the embedded triangle, as illustrated in Fig. 9. To estimate the uncovered surface area, we need width of beams, which is given by $(2\epsilon + 1)$ with ϵ being the thickness. Then, the base length of this inner triangle is

$$\frac{8D}{|\mathcal{B}|} - (2\epsilon + 1). \quad (13)$$

Using a trigonometric ratio for orthogonal triangles the height of the triangle can be computed by

$$\frac{\frac{8D}{|\mathcal{B}|} - (2\epsilon + 1)}{\tan(\gamma)}. \quad (14)$$

Then, the uncovered surface area is approximately

$$\Delta'(|\mathcal{B}|, D) \approx \frac{1}{2} \frac{\frac{8D}{|\mathcal{B}|} - (2\epsilon + 1)}{\tan(\gamma)} \left(\frac{8D}{|\mathcal{B}|} - (2\epsilon + 1) \right) \approx \frac{\left(\frac{8D}{|\mathcal{B}|} - (2\epsilon + 1) \right)^2}{2 \tan(\gamma)}. \quad (15)$$

Adding together the beam thickness and the uncovered area and subtracting the overall surface area gives the overlap

$$\Gamma_{\Delta}^{(\text{over})}(|\mathcal{B}|, D) \approx (2\epsilon + 1)D + \Delta'(|\mathcal{B}|, D) - \Delta(|\mathcal{B}|, D). \quad (16)$$

This allows us to compute the coverage by subtracting this overlap from the beam thickness

$$\Gamma_{\Delta}^{(\text{cover})}(|\mathcal{B}|, D) \approx (2\epsilon + 1)D - \Gamma_{\Delta}^{(\text{over})}(|\mathcal{B}|, D). \quad (17)$$

Due to the linear relaxation and the partitioning of the area in equivalent triangles, a linear extrapolation to the full image is possible. Such that, the total overlap and coverage are given by

$$\begin{aligned} \Gamma_{\text{over}}(|\mathcal{B}|, D) &\approx |\mathcal{B}| \Gamma_{\Delta}^{(\text{over})}(|\mathcal{B}|, D) \\ &\approx |\mathcal{B}| [(2\epsilon + 1)D + \Delta'(|\mathcal{B}|, D) - \Delta(|\mathcal{B}|, D)] \\ &\approx |\mathcal{B}| \left[(2\epsilon + 1)D + \frac{\left(\frac{8D}{|\mathcal{B}|} - (2\epsilon + 1)\right)^2}{2\tan(\gamma)} - \frac{4D^2}{|\mathcal{B}|} \right], \end{aligned} \quad (18)$$

$$\begin{aligned} \Gamma_{\text{cover}}(|\mathcal{B}|, D) &\approx |\mathcal{B}| \Gamma_{\Delta}^{(\text{cover})}(|\mathcal{B}|, D) \\ &\approx |\mathcal{B}| [(2\epsilon + 1)D - (2\epsilon + 1)D - \Delta'(|\mathcal{B}|, D) + \Delta(|\mathcal{B}|, D)] \\ &\approx |\mathcal{B}| \left[\frac{4D^2}{|\mathcal{B}|} - \frac{\left(\frac{8D}{|\mathcal{B}|} - (2\epsilon + 1)\right)^2}{2\tan(\gamma)} \right]. \end{aligned} \quad (19)$$

Both approximations ground on the assumption of triangles and thus subject to $|\mathcal{B}| \geq 8$. \square

D.2 Maximal Beam Set Cardinality

Proof. Each beam needs to cover at least one pixel not covered by others, otherwise these beams would be redundant. We say that the maximum number of beams $|\mathcal{B}_{max}|$ is reached if the receptive field fully covers the image. Therefore, we use the coverage approximation from Lemma 1

$$\Gamma_{\text{cover}}(|\mathcal{B}|, D) \approx |\mathcal{B}| \left[\frac{4D^2}{|\mathcal{B}|} - \frac{\left(\frac{8D}{|\mathcal{B}|} - (2\epsilon + 1)\right)^2}{2\tan(\gamma)} \right].$$

To obtain $|\mathcal{B}_{max}|$ we compute the derivation *w.r.t.* $|\mathcal{B}|$, such that

$$\begin{aligned} \frac{\partial \Gamma_{\text{cover}}(|\mathcal{B}|, D)}{\partial |\mathcal{B}|} &= \frac{64D^2}{|\mathcal{B}|^2} - (2\epsilon + 1)^2 \frac{1}{2\tan(\gamma)} = 0 \\ |\mathcal{B}| &= \sqrt{\frac{64D^2}{(2\epsilon + 1)^2}} \approx |\mathcal{B}_{max}|. \end{aligned} \quad (20)$$

For $\epsilon = 0$ this gives exact maximas. For $\epsilon \geq 1$ the integer constraint for the cardinality is violated and we have an approximation for the true $|\mathcal{B}_{max}|$. \square

D.3 Optimal Padding Margin

Proof. Let $W \in \mathbb{N}$ and $H \in \mathbb{N}$ denote the width and height, respectively, of an squared image X with $W = H$. This sets the center point at $\mathbf{c} = [W/2, W/2]$. The image can be zero padded uniformly at the borders by a margin $\delta \in \mathbb{N}$. The goal is to find δ such that any arbitrary rotation of the image around its center will not cause any information loss. Information is lost if any pixel of X , which is bounded spatially by the unpadded vanilla image region, gets rejected during rotation. Using a rotation matrix $R \in [1, -1]^4$ pixel vectors are mapped to real vectors. When enforcing the rigid discrete pixel grid, pixels might get cut off. Let \mathbf{d} be the maximal distant pixel from \mathbf{c} , which clearly lies in the corners of the image. By the Pythagorean theorem we have $\|\mathbf{d}\|_2 = \sqrt{(W/2)^2 + (H/2)^2} = \sqrt{2}(W/2)$ using the assumption above. The cut off is maximal if the image is rotated by 45° and hence \mathbf{d} is orthogonal

to the width and height axes. So, the required padding can be quantified by the ceiled offset between $\|\mathbf{d}\|_2$ and $W/2$ such that

$$\delta = \lceil \max\left(0, \left\lceil \|\mathbf{d}\|_2 - \frac{W}{2} \right\rceil \right) = \max\left(0, \left\lceil \sqrt{2} \frac{W}{2} - \frac{W}{2} \right\rceil \right) = \max\left(0, \left\lceil \frac{1}{2} W (\sqrt{2} - 1) \right\rceil \right). \quad (21)$$

□

E Loss Analysis

E.1 Circle Loss preserves Angle Distances

One-dimensional real values lie on the number line \mathbb{R} or on a subset of it if bounds apply. This renders distance measuring trivial, *e.g.* we might use the absolute difference between two scalars. Angles, on the other hand, lie on a circle, such that 0° and 359° are closer as 0° and 2° . We show that our circle loss

$$\mathcal{L}_{\text{circle}}(\theta, \mathbf{z}) = (\sin(\theta) - \text{im}(\mathbf{z}))^2 + (\cos(\theta) - \text{re}(\mathbf{z}))^2$$

preserves angle distances and is therefore highly expressive. It is well known, that the minimum and maximum numerical angle values are 0° and 360° , respectively. Let $d(\theta, \theta') \in \mathbb{R}_+$ be a distance measure between two arbitrary angles θ and θ' . We seek a distance measure where the following two conditions holds

$$\lim_{\theta \rightarrow 360^\circ} d(\theta, 0^\circ) = 0, \quad (22)$$

$$\lim_{\theta \rightarrow 0^\circ} d(\theta, 360^\circ) = 0. \quad (23)$$

Using our circle loss it is easy to show that both conditions hold, *i.e.*

$$\begin{aligned} \lim_{\theta \rightarrow 360^\circ} (\sin(0^\circ) - \sin(\theta))^2 + (\cos(0^\circ) - \cos(\theta))^2 \\ = (\sin(0^\circ) - \sin(360^\circ))^2 + (\cos(0^\circ) - \cos(360^\circ))^2 = 0, \end{aligned} \quad (24)$$

$$\begin{aligned} \lim_{\theta \rightarrow 0^\circ} (\sin(360^\circ) - \sin(\theta))^2 + (\cos(360^\circ) - \cos(\theta))^2 \\ = (\sin(360^\circ) - \sin(0^\circ))^2 + (\cos(360^\circ) - \cos(0^\circ))^2 = 0. \end{aligned} \quad (25)$$

Therefore, we conclude that our circle loss indeed respects the angle distances.

E.2 Extrema Analysis

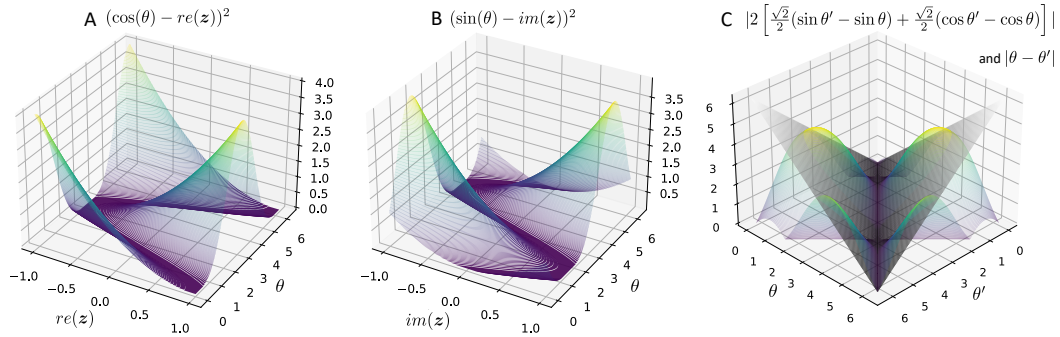


Figure 10: **A** and **B** illustrate both loss term surface plots, while **C** depicts the plot of both Lipschitz relevant inequality terms with $\text{im}(z), \text{re}(z) = \sqrt{2}/2$.

For an extrema analysis we first derive the partial derivatives of the multivariable loss

$$\mathcal{L}_{\text{circle}}(\theta, \mathbf{z}) = (\sin(\theta) - \text{im}(\mathbf{z}))^2 + (\cos(\theta) - \text{re}(\mathbf{z}))^2.$$

The input lies in the cubic domain bounded by $\hat{\theta} \in [0, 2\pi)$ and $\mathbf{z} \in [-1, 1]^2$. The gradient is given by

$$\nabla \mathcal{L}_{\text{circle}}(\theta, \mathbf{z}) = \left[\frac{\partial \mathcal{L}_{\text{circle}}(\theta, \mathbf{z})}{\partial \theta}, \frac{\partial \mathcal{L}_{\text{circle}}(\theta, \mathbf{z})}{\partial \text{re}(\mathbf{z})}, \frac{\partial \mathcal{L}_{\text{circle}}(\theta, \mathbf{z})}{\partial \text{im}(\mathbf{z})} \right]^\top. \quad (26)$$

This resolves in

$$\begin{aligned} \frac{\partial}{\partial \theta} \mathcal{L}_{circle}(\theta, \mathbf{z}) &= 2\cos(\theta)(\sin(\theta) - im(\mathbf{z})) - 2\sin(\theta)(\cos(\theta) - re(\mathbf{z})) \\ &= 2[re(\mathbf{z})\sin(\theta) - im(\mathbf{z})\cos(\theta)], \end{aligned} \quad (27)$$

$$\frac{\partial}{\partial re(\mathbf{z})} \mathcal{L}_{circle}(\theta, \mathbf{z}) = 2(\cos(\theta) - re(\mathbf{z})), \quad (28)$$

$$\frac{\partial}{\partial im(\mathbf{z})} \mathcal{L}_{circle}(\theta, \mathbf{z}) = 2(\sin(\theta) - im(\mathbf{z})). \quad (29)$$

Analysing the behaviour of Eq. (28) and Eq. (29) at zero indicates that a critical function is given at $im(\mathbf{z}) = \sin(\theta)$ and $re(\mathbf{z}) = \cos(\theta)$. We provided a visual support in Fig. 10, where we plotted both loss terms of Eq. (8). The minimas lie along \sin and \cos . Intuitively, due to the squares in Eq. (8) and the sum operation as loss term concatenation, there is no room for other minimas. Since predictions and ground truth values have numerical bounds, the loss is upper bounded as well. To quantify this upper bound, we aim to solve

$$\theta^*, \mathbf{z}^* = \underset{\theta, \mathbf{z}}{\operatorname{argmax}} \mathcal{L}_{circle}(\theta, \mathbf{z}). \quad (30)$$

We maximize the loss by using diametrical unit vector predictions compared to the ground truth, *i.e.*, $im(\mathbf{z})^* = \cos(\theta)$ and $re(\mathbf{z})^* = \sin(\theta)$. This leads to

$$\theta^* = \underset{\theta}{\operatorname{argmax}} (\sin(\theta) - \cos(\theta))^2 + (\cos(\theta) - \sin(\theta))^2 = \frac{3}{4}\pi. \quad (31)$$

So, we have the upper bound $\mathcal{L}_{circle}(\frac{3}{4}\pi, [\sin(\theta^*), \cos(\theta^*)]) = 4$.

E.3 Lipschitz Smoothness

Our loss function is Lipschitz smooth *iff* the following condition hold

$$\|\mathcal{L}_{circle}(\theta, \mathbf{z}) - \mathcal{L}_{circle}(\theta', \mathbf{z})\| \leq K\|\theta - \theta'\|, \quad (32)$$

where K is the Lipschitz constant. Using the definition of the loss in Eq. (8) gives

$$\begin{aligned} &\|(\sin(\theta) - im(\mathbf{z}))^2 + (\cos(\theta) - re(\mathbf{z}))^2 - \\ &(\sin(\theta') - im(\mathbf{z}))^2 - (\cos(\theta') - re(\mathbf{z}))^2\| \leq K\|\theta - \theta'\|. \end{aligned} \quad (33)$$

This dissolves in

$$\begin{aligned} &\|\sin^2(\theta) - 2im(\mathbf{z})\sin(\theta) + im(\mathbf{z})^2 + \\ &\cos^2(\theta) - 2re(\mathbf{z})\cos(\theta) + re(\mathbf{z})^2 - \\ &\sin^2(\theta') + 2im(\mathbf{z})\sin(\theta') - im(\mathbf{z})^2 - \\ &\cos^2(\theta') + 2re(\mathbf{z})\cos(\theta') - re(\mathbf{z})^2\| \leq K\|\theta - \theta'\|. \end{aligned} \quad (34)$$

Using the trigonometrical identity $\sin^2(\theta) + \cos^2(\theta) = 1$ and some rearrangements give

$$\|2[im(\mathbf{z})(\sin(\theta') - \sin(\theta)) + re(\mathbf{z})(\cos(\theta') - \cos(\theta))]\| \leq K\|\theta - \theta'\|. \quad (35)$$

Assuming no trivial case, *i.e.*, $\theta \neq \theta'$, the projection on the unit circle gives always smaller norms

$$\|\sin(\theta') - \sin(\theta)\| < \|\theta - \theta'\|, \quad (36)$$

$$\|\cos(\theta') - \cos(\theta)\| < \|\theta - \theta'\|. \quad (37)$$

Furthermore, per definition we have $\|\mathbf{z}\| = 1$, thus only a fraction of both terms above are aggregated. With $K = 2$ the Lipschitz inequality can be guaranteed. In Fig. 10C we plotted both functions of the inequality.

F BIC Layer Specification

We offer different levels of technical insight. The methodological fundamentals of BIC are given in Section Sec. 4. We provide further details about the implementation in Section Sec. 5, which are picked up in this section. These technical levels are eventually closed by the open-sourced code going along with this paper.

F.1 Beam Encoder

We partitioned the beam encoder into a proximity encoder and a spatial encoder to have a clean semantic separation. The receptive field of the proximity encoder covers the local spatial neighborhood of pixels. The proximity is compressed $\mathbb{R}^{2\epsilon+1 \times D \times C} \rightarrow \mathbb{R}^{D-8 \times L/8}$ by two-dimensional convolutional kernels. Find the layer specifications in Table 2. Then, the remaining spatial pixel information is encoded by one-dimensional convolutional kernels, mapping $\mathbb{R}^{D-8 \times L/8} \rightarrow \mathbb{R}^L$. Due to the compression the architecture of the spatial encoder is sensitive to D . We provide details of such encoders in Table 3, Table 4, Table 5, and Table 6. For all layers we aim to preserve the spatial ordering of features and hence no explicit pooling layers are used. This originates from the fact that for rotational perturbation detection the further pixels are from the center the more information they convey. Pixels close to the center not only hold redundancies due to the overlaps but also follow smaller rotation circles and hence pixels are less sensitive to minor rotations.

Table 2: The proximity encoder for $\epsilon = 1$ and with $|\mathcal{B}| > 8$.

Layer	Kernel	Padding	Strides	Non-Linearity	Feature Maps
1	(3, 3)	no	1	LeakyReLU	L/8

Table 3: The spatial encoder for 28×28 images with $|\mathcal{B} = 14|$, e.g., from *FashionMNIST*.

Layer	Kernel	Padding	Strides	Non-Linearity	Feature Maps
1	4	no	1	LeakyReLU	L/4
2	4	no	1	LeakyReLU	L/2
3	4	no	1	LeakyReLU	L/2
4	3	no	1	LeakyReLU	L

Table 4: The spatial encoder for 32×32 images with $|\mathcal{B} = 16|$, e.g., from *CIFAR10*.

Layer	Kernel	Padding	Strides	Non-Linearity	Feature Maps
1	4	no	1	LeakyReLU	L/4
2	4	no	1	LeakyReLU	L/2
3	4	no	1	LeakyReLU	L/2
4	4	no	1	LeakyReLU	L
5	2	no	1	LeakyReLU	L

Table 5: The spatial encoder for 128×128 images with $|\mathcal{B} = 64|$, e.g., from *COIL100*.

Layer	Kernel	Padding	Strides	Non-Linearity	Feature Maps
1	5	no	2	LeakyReLU	L/4
2	4	no	2	LeakyReLU	L/4
3	4	no	1	LeakyReLU	L/2
4	4	no	1	LeakyReLU	L/2
5	4	no	1	LeakyReLU	L/2
6	3	no	1	LeakyReLU	L
7	2	no	1	LeakyReLU	L

F.2 Context Encoder

We build upon the fundamentals provided in Sec. 4. The graph topology allows for a controllable and scalable information exchange between neighbors controlled by the number of layers, i.e., the number of hops. Since the ordering of neighbors matters in our case directed edges are used to circumvent the permutation invariance of GNNs (Graph Neural Networks) [17, 18, 31]. For simplicity sake, we update nodes by $\lambda Af(\mathcal{B})W$, where $f(\mathcal{B})$ is the output of the beam encoder, $A \in \{0, 1\}^{|\mathcal{B}| \times |\mathcal{B}|}$ is the

Table 6: The spatial encoder for 250×250 images with $|\mathcal{B}| = 125$, e.g., from *LFW*.

Layer	Kernel	Padding	Strides	Non-Linearity	Feature Maps
1	4	no	2	LeakyReLU	L/4
2	3	no	2	LeakyReLU	L/4
3	4	no	2	LeakyReLU	L/4
4	4	no	1	LeakyReLU	L/2
5	4	no	1	LeakyReLU	L/2
6	4	no	1	LeakyReLU	L/2
7	3	no	1	LeakyReLU	L
8	2	no	1	LeakyReLU	L

binary adjacency matrix and $W \in \mathbb{R}^{L \times L}$ is the learnable weight matrix. To limit the impact of neighbor information, we use $\lambda \in (0, 1]$ as a global edge factor. For the proposed directed wheel graph we have an adjacency matrix

$$A = \begin{bmatrix} 0 & 1 & 0 & 0 & \dots & 1 \\ 0 & 0 & 1 & 0 & \dots & 1 \\ 0 & 0 & 0 & 1 & \dots & 1 \\ 0 & 0 & 0 & 0 & \dots & 1 \\ \vdots & \vdots & \vdots & \vdots & \ddots & \vdots \\ 1 & 0 & 0 & 0 & \dots & 1 \end{bmatrix}. \quad (38)$$

G Experimental Setups

G.1 *t-SNE* Parameters

For dimensionality reduction we utilize t-Distributed Stochastic Neighbor Embeddings (t-SNE). We use the `sklearn` implementation of *t-SNE* with an Barnes-Hut approximation for 1000 iterations. We use a random initialization, a perplexity of 30, early exaggeration of 12 and the Euclidean metric. An automatic learning rate ρ is used, such that $\rho = \max(\frac{n}{0.25 \text{early_exaggeration}}, 50)$, where n is the sample size. Further, a minimum gradient norm of $1e-7$ for early stopping is utilized. We trained our BIC model using the setup given in Sec. 5. The model was trained on *COIL100* using $\mathcal{C}_{|\mathcal{B}|}$ without the Toeplitz prior. We used the beam embeddings from the beam encoder without the context integration to avoid bias. A spectral color schema to illustrate the $|\mathcal{B}| = 32$ beams is employed for the visual purposes.